NASA TM-100664

NASA-TM-100664 19880019508

NASA Technical Memorandum 100664

ACCURATE SOLUTIONS, PARAMETER STUDIES, AND COMPARISONS FOR THE EULER AND POTENTIAL FLOW EQUATIONS

W. KYLE ANDERSON
JOHN T. BATINA

SEPTEMBER 1988

NASA
National Aeronautics and
Space Administration

Langley Research Center
Hampton, Virginia 23665-5225

ACCURATE SOLUTIONS, PARAMETER STUDIES, AND COMPARISONS FOR THE EULER AND POTENTIAL FLOW EQUATIONS

W. Kyle Anderson
John T. Batina

NASA Langley Research Center
Hampton, Virginia

ABSTRACT

Parameter studies are conducted using the Euler and potential flow equation models for steady and unsteady flows in both two and three dimensions. The Euler code is an implicit, upwind, finite volume code which uses the Van Leer method of flux-vector-splitting which has been recently extended for use on dynamic meshes and maintains all the properties of the original splitting. The potential flow code is an implicit, finite difference method for solving the transonic small-disturbance (TSD) equations and incorporates both entropy and vorticity corrections into the solution procedure thereby extending its applicability into regimes where shock strength normally precludes its use. Parameter studies resulting in benchmark type calculations include the effects of spatial and temporal refinement, spatial order of accuracy, far field boundary conditions for steady flow, frequency of oscillation, and the use of subiterations at each time step to reduce linearization and factorization errors. Comparisons between Euler and potential flow results are made as well as with experimental data where available.

INTRODUCTION

Considerable progress has been made over the past two decades on developing computational fluid dynamics (CFD) methods for steady and unsteady flow analysis. Two recent surveys which summarize much of this progress are given in Refs. 1 and 2. Jameson,[1] for example, has discussed successes and challenges in computational aerodynamics with emphasis on steady flow applications. Edwards and Thomas,[2] have reviewed computational methods for unsteady transonic flows with emphasis on applications to aeroelastic analysis and flutter prediction. Applications of CFD methods have become relatively commonplace in recent years, for a wide range of fluid flow problems. These applications have met with varying degrees of success, however, due to various deficiencies in the numerical modeling. These deficiencies include: an insufficient number of grid points to resolve the physics of the flow, an insufficient grid extent for external flow problems, too large of a time step to accurately capture the unsteadiness of the flow, and inaccurate boundary conditions, to name but a few. Consequently, the methods require further evaluation by performing detailed studies to assess the influence of each parameter in the numerical modeling on the solution. Through such studies, the accuracy and hence applicability of the methods may be determined.

Because of increased computer speed and memory available on current supercomputers, it is now timely to pursue such validation studies. Therefore, the purpose of the present paper is to report some results of such a study, performed using the Euler equations and the transonic small-disturbance (TSD) potential equation. Descriptions of the governing equations and numerical methods of solution are given first. Parameter studies for steady flow applications are presented next which show the effects of grid density, spatial accuracy, and far field boundary conditions. Parameter studies for unsteady flow applications are also presented which show the effects of reduced frequency, time step size, and the use of performing subiterations to minimize linearization and factorization errors in the time-accurate calculations. Comparisons of the TSD solutions with the Euler solutions are given to assess the applicability of the TSD potential flow method. In the TSD solutions, entropy and vorticity effects are accounted for to more accurately treat cases with strong shock waves. Finally, the results are validated by making comparisons with available experimental steady and unsteady data.

COMPUTATIONAL PROCEDURES

In this section, the computational procedures are described including the governing equations and the numerical method of solution for both the Euler equations and the transonic small-disturbance equation.

Euler Code

Governing Equations

The governing equations are the time-dependent equations of ideal gas dynamics, i.e. the Euler equations, which express the conservation of mass, momentum, and energy for an inviscid gas. The equations are written in generalized coordinates and conservation form:

$$\frac{\partial \hat{Q}}{\partial t} + \frac{\partial \hat{F}}{\partial \xi} + \frac{\partial \hat{G}}{\partial \eta} + \frac{\partial \hat{H}}{\partial \zeta} = 0 \tag{1}$$

where

$$\hat{Q} = \frac{Q}{J} = \frac{1}{J}\begin{bmatrix} \rho \\ \rho u \\ \rho v \\ \rho w \\ e \end{bmatrix} \tag{2}$$

$$\hat{F} = \frac{1}{J}\begin{bmatrix} \rho U \\ \rho U u + \xi_x p \\ \rho U v + \xi_y p \\ \rho U w + \xi_z p \\ (e+p)U - \xi_t p \end{bmatrix} \tag{3}$$

N88-28892 #

$$\hat{G} = \frac{1}{J}\begin{bmatrix} \rho V \\ \rho V u + \eta_x p \\ \rho V v + \eta_y p \\ \rho V w + \eta_z p \\ (e+p)V - \eta_t p \end{bmatrix} \tag{4}$$

$$\hat{H} = \frac{1}{J}\begin{bmatrix} \rho W \\ \rho W u + \varsigma_x p \\ \rho W v + \varsigma_y p \\ \rho W w + \varsigma_z P \\ (e+p)W - \varsigma_t p \end{bmatrix} \tag{5}$$

$$\begin{aligned} U &= \xi_x u + \xi_y v + \xi_z w + \xi_t \\ V &= \eta_x u + \eta_y v + \eta_z w + \eta_t \\ W &= \varsigma_x u + \varsigma_y v + \varsigma_z w + \varsigma_t \end{aligned} \tag{6}$$

$$p = (\gamma - 1)[e - \rho(u^2 + v^2 + w^2)/2] \tag{7}$$

The variables ξ and η correspond to the coordinates parallel and normal to the body surface, respectively, while ς corresponds to the spanwise direction for three dimensional flow. Q represents density, momentum, and total energy per unit volume. The Jacobian of the transformation, J, is defined as:

$$J = \frac{\partial(\xi, \eta, \varsigma)}{\partial(x, y, z)} \tag{8}$$

The equations are nondimensionalized by the freestream density $\tilde{\rho}_\infty$ and soundspeed $\tilde{a}_\infty$.

Numerical Method

The Euler code used in the present study is the CFL3D code developed in the Analytical Methods Branch at NASA Langley Research Center.[3,4] This is an implicit, finite volume, upwind-differencing code in which the spatial derivatives of the fluxes are split into forward and backward contributions using flux-vector splitting so that type dependent differencing can be utilized. The flux-vector splitting method used is that of Van Leer,[5,6] which has been recently extended for use on dynamic meshes.[4] It is continuously differentiable at eigenvalue sign changes and allows shocks to be captured with at most two interior zones. In practice, only one zone is usually observed.

Although flux-vector splitting is used in the current study, the code also incorporates the flux-difference approach of Roe.[6] The code can be used for steady and unsteady flows using either the Euler or Navier Stokes equations and can handle very general geometries since it allows for block structured and embedded grids.

The starting point for the time advancement algorithm is the backward Euler time differencing scheme:

$$R(Q^{n+1}) = 0 \tag{9}$$

where $R(Q^{n+1})$ is given by:

$$\left[\delta_\xi \hat{F} + \delta_\eta \hat{G} + \delta_\varsigma \hat{H}\right]^{n+1} + \left[\frac{(1+\phi)}{J\Delta t} Q^{n+1} - \frac{(1+2\phi)}{J\Delta t} Q^n + \frac{\phi}{J\Delta t} Q^{n-1}\right] = 0 \tag{10}$$

If $\phi = 0$, the scheme is first-order accurate in time, while if $\phi = 1/2$, the scheme is temporally second-order accurate.

The flux-vector splitting (FVS) method extended for dynamic meshes in Ref. 4 is used to split the fluxes into forward and backward contributions according to the signs of the eigenvalues of the Jacobian matrices. For example, $\delta_\xi \hat{F}$ in Eq. (10) at a cell centered at point i (holding the j and k indices constant) can be written:

$$\begin{aligned} \left[\delta_\xi \hat{F}\right]_i &\equiv \left[\delta_\xi^- \hat{F}^+ + \delta_\xi^+ \hat{F}^-\right]_i \\ &= \left[\hat{F}^+(Q^-_{i+1/2}) + \hat{F}^-(Q^+_{i+1/2})\right] - \\ &\quad \left[\hat{F}^+(Q^-_{i-1/2}) + \hat{F}^-(Q^+_{i-1/2})\right] \end{aligned} \tag{11}$$

The equations for $\hat{F}^{\pm}$ for a moving mesh can be found in Ref. 4. $Q^{\pm}$ denotes state variables on cell interfaces determined from upwind-biased interpolations of the conserved variables.

$$Q^{-}_{i+1/2} = Q_i + \left\{\frac{1}{4}[(1-\kappa)\Delta_- + (1+\kappa)\Delta_+]\right\}_i \tag{12a}$$

$$Q^{+}_{i+1/2} = Q_{i+1} - \left\{\frac{1}{4}[(1-\kappa)\Delta_+ + (1+\kappa)\Delta_-]\right\}_{i+1} \tag{12b}$$

where

$$\Delta_+ = Q_{i+1} - Q_i \qquad \Delta_- = Q_i - Q_{i-1} \tag{13}$$

The parameter $\kappa \in [-1, 1]$ forms a family of difference schemes[5]: $\kappa = -1$ corresponds to second-order fully-upwind differencing, $\kappa = 0$ to Fromms scheme, and $\kappa = 1/3$ to third-order upwind-biased differencing.

When flux-limiting is desired to eliminate oscillations in shock regions, a *min-mod* limiter is used. Flux-limited interpolations are identical in form to Eqs. (12a) and (12b), except that Δ_+ and Δ_- are replaced with $\overline{\Delta}_+$ and $\overline{\Delta}_-$, respectively, where:

$$\begin{aligned} \overline{\Delta}_+ &= \max\left[0, \min(\Delta_+ \mathrm{sgn}\Delta_-, \beta\Delta_- \mathrm{sgn}\Delta_+)\right]\mathrm{sgn}\Delta_+ \\ \overline{\Delta}_- &= \max\left[0, \min(\Delta_- \mathrm{sgn}\Delta_+, \beta\Delta_+ \mathrm{sgn}\Delta_-)\right]\mathrm{sgn}\Delta_- \end{aligned} \tag{14}$$

$$\beta = \frac{(3-\kappa)}{(1-\kappa)} \tag{15}$$

Equation (9) is a nonlinear equation which can be solved iteratively using a Newton linearization as

$$\frac{\partial R}{\partial Q}(Q^{\ell+1} - Q^{\ell}) = -R(Q^{\ell}) \tag{16}$$

Here, ℓ is a sequence of iterates so that at convergence $Q^{\ell+1} = Q^{\ell} = Q^{n+1}$. The solution of Eq. (16) at each time step is generally not feasible, however, since it requires the solution of a large banded matrix. The solution is therefore obtained with a spatially-split approximate factorization, in which the implicit operator is split into a sequence of easily invertible equations. The three-dimensional algorithm is implemented in three steps as:

$$\begin{aligned} \left[\frac{I(1+\phi)}{J\Delta t} + \delta^{-}_{\xi}\frac{\partial \hat{F}^{+}}{\partial Q} + \delta^{+}_{\xi}\frac{\partial \hat{F}^{-}}{\partial Q}\right]\Delta Q^{*} &= -R(Q^{\ell}) \\ \left[\frac{I(1+\phi)}{J\Delta t} + \delta^{-}_{\eta}\frac{\partial \hat{G}^{+}}{\partial Q} + \delta^{+}_{\eta}\frac{\partial \hat{G}^{-}}{\partial Q}\right]\Delta Q^{**} &= \left(\frac{1+\phi}{J\Delta t}\right)\Delta Q^{*} \\ \left[\frac{I(1+\phi)}{J\Delta t} + \delta^{-}_{\zeta}\frac{\partial \hat{H}^{+}}{\partial Q} + \delta^{+}_{\zeta}\frac{\partial \hat{H}^{-}}{\partial Q}\right]\Delta Q^{\ell} &= \left(\frac{1+\phi}{J\Delta t}\right)\Delta Q^{**} \\ Q^{l+1} &= Q^{l} + \Delta Q^{\ell} \end{aligned} \tag{17}$$

For time accurate calculations, successive iterations of Eq. (17) can be used at each time step in order to minimize factorization and linearization errors.

For steady state calculations, only one iteration of Eq. (17) is used at each step. In addition, the convergence rate is accelerated using a local time stepping procedure and the FAS multigrid scheme.[3] The implicit spatial derivatives of the convective and pressure terms are spatially first-order accurate, resulting in block tridiagonal inversions for each sweep. The algorithm is completely vectorizable since the operations in each of the spatial directions can be vectorized over the remaining two.

At each time step boundary conditions are applied explicitly. In the far field, a quasi-one-dimensional characteristic analysis is used to determine boundary data, while on the body, pressure and density are extrapolated from the interior and no flow is allowed through the surface.

Potential Code

Governing Equations

In the potential flow calculations, the flow is assumed to be governed by the general frequency, modified TSD potential equation which may be written in conservation law form as

$$\frac{\partial f_0}{\partial t} + \frac{\partial f_1}{\partial x} + \frac{\partial f_2}{\partial y} + \frac{\partial f_3}{\partial z} = 0 \tag{18}$$

where

$$\begin{aligned} f_0 &= -A\phi_t - B\phi_x \\ f_1 &= E\phi_x + F{\phi_x}^2 + G{\phi_y}^2 \\ f_2 &= \phi_y + H\phi_x\phi_y \\ f_3 &= \phi_z \end{aligned} \tag{19}$$

The coefficients A, B, and E are defined as

$$A = M_\infty^2 \qquad B = 2M_\infty^2 \qquad E = 1 - M_\infty^2 \tag{20}$$

Several choices are available for the coefficients F, G, and H depending upon the assumptions used in deriving the TSD equation. The coefficients herein are defined as

$$F = -\frac{1}{2}(\gamma+1)M_\infty^2 \quad G = \frac{1}{2}(\gamma-3)M_\infty^2 \quad H = -(\gamma-1)M_\infty^2 \tag{21}$$

The lifting surface is modeled by imposing the following boundary conditions:

$$Flow \quad tangency : {\phi_z}^{\pm} = {f_x}^{\pm} + f_t \tag{22a}$$

$$Trailing \quad wake : \Gamma_t + \Gamma_x = 0 \qquad and \qquad \Delta\phi_z = 0 \tag{22b}$$

where $\Delta(\ )$ represents the jump in $(\ )$ across the wake. The flow-tangency condition is imposed along the mean plane of the lifting surface. In Eq. (22a) the plus and minus superscripts indicate the upper and lower surfaces of the mean plane, respectively. The wake is assumed to be a planar extension from the trailing edge to the downstream boundary of the finite-difference grid.

Entropy effects are included in the TSD solution[7] by replacing the streamwise flux f_1 (Eq. (19)) in the TSD equation by an alternative flux given by

$$f_1 = (\gamma+1)M_\infty^2 R(V\bar{V} - \frac{1}{2}V^2) + G{\phi_y}^2 \tag{23}$$

where

$$R = \left[\frac{2 + (\gamma-1)M_\infty^2}{(\gamma+1)M_\infty^2}\right]^{\frac{1}{2}} \tag{24a}$$

$$V = \left[\frac{(1+R)\phi_x}{1 + \phi_x + R}\right] \tag{24b}$$

$$\bar{V} = \left[\frac{R^2 - 1}{2R}\right] \tag{24c}$$

The first term of this new flux was derived by an asymptotic expansion of the Euler equations including the effects of shock-generated entropy. This analysis shows that Eq. (23) is accurate to at least $O({\phi_x}^3)$ in the expanded Euler equations.

Vorticity effects are included in the TSD solution[7] by writing the velocity vector as the sum of potential and rotational components according to

$$\vec{V} = \nabla\Phi - \frac{1}{\gamma - 1}\frac{s}{c_v}\nabla\Psi \tag{25}$$

In Eq. (25), the first term on the right-hand side is the gradient of a scalar potential Φ and the second term involves the product of the entropy s and the gradient of a Clebsch variable Ψ. The function Ψ is a measure of the stretching and rotating of vortex filaments associated with entropy variation.[8] For the applications of interest in the present work, the rotational part of the velocity vector is assumed to occur only in the region downstream of shock waves. Further assuming that the entropy convects with the freestream speed and that the shock curvature is negligible implies that

$$\frac{\partial \Psi}{\partial x} = \frac{1}{\gamma M_\infty^2}, \qquad \frac{\partial \Psi}{\partial y} = 0, \qquad \frac{\partial \Psi}{\partial z} = 0 \tag{26}$$

as shown in Ref. 8. These assumptions eliminate the variable Ψ from the formulation leaving only the entropy to be determined throughout the flow field. In a steady flow, entropy is constant along streamlines and changes only through shock waves. The entropy jump is computed along shocks using the Rankine-Hugoniot relation

$$\frac{s}{c_v} = ln\frac{(\gamma+1)u_1{}^2 - (\gamma-1)R^2}{(\gamma+1)R^2 - (\gamma-1)u_1{}^2} - \gamma ln\frac{u_1{}^2}{R^2} \tag{27}$$

where

$$u_1 = 1 + \phi_x - u_s \tag{28}$$

In Eq.(28), u_1 is the flow speed upstream of the shock and u_s is the shock speed. Then, for simplicity, the grid lines are assumed to approximate the streamlines of the flow, which is consistent with the small-disturbance approximation. The entropy is either convected downstream along the grid lines according to

$$\frac{\partial s}{\partial t} + \frac{\partial s}{\partial x} = 0 \tag{29}$$

for unsteady applications, or is held constant along the grid lines for steady applications.

The modified velocity vector in turn modifies the TSD equation because the streamwise disturbance speed $u = \phi_x$ is now given by

$$u = \phi_x - \frac{1}{\gamma(\gamma-1)M_\infty^2}\frac{s}{c_v} \tag{30}$$

The new TSD equation has the same conservation law form as Eq. (18) with the new fluxes defined by simply replacing ϕ_x by the modified speed given by Eq. (30).

Numerical Method

The potential flow code used in the present study is the CAP-TSD code developed in the Unsteady Aerodynamics Branch at NASA Langley Research Center.[9,10] The code uses a time-accurate approximate factorization (AF) algorithm similar to that described previously for the Euler equations, for the solution of the TSD equation.[11,12] The AF algorithm consists of a Newton linearization procedure coupled with an internal iteration technique. For unsteady flow calculations, the solution procedure involves two steps. First, a time linearization step is performed to determine an estimate of the potential field. Second, internal iterations are performed to minimize linearization and factorization errors. Specifically, the TSD equation (Eq. (18)) is written in general form as

$$R(\phi^{n+1}) = 0 \tag{31}$$

where ϕ^{n+1} represents the unknown potential field at time level (n+1). The solution to Eq. (31) is then given by the Newton linearization of Eq. (31) about ϕ^ℓ

$$R(\phi^\ell) + \left(\frac{\partial R}{\partial \phi}\right)_{\phi=\phi^\ell} \Delta\phi = 0 \tag{32}$$

In Eq. (32), ϕ^ℓ is the currently available value of ϕ^{n+1} and $\Delta\phi = \phi^{\ell+1} - \phi^\ell$. During convergence of the iteration procedure, $\Delta\phi$ will approach zero so that the solution will be given by $\phi^{n+1} = \phi^\ell$. In general, only one or two iterations are required to achieve acceptable convergence.

The AF algorithm is formulated by first approximating the time derivative terms (ϕ_{tt} and ϕ_{xt} terms) by second-order accurate finite-difference formulae. The TSD equation is rewritten by substituting $\phi = \phi^\ell + \Delta\phi$ and neglecting squares of derivatives of $\Delta\phi$ which is equivalent to applying Eq. (32) term by term. The resulting equation is then rearranged and the left-hand side is approximately factored into a triple product of operators yielding

$$L_\xi L_\eta L_\varsigma \Delta\phi = -\sigma R(\phi^\ell, \phi^n, \phi^{n-1}, \phi^{n-2}) \tag{33}$$

where

$$\begin{aligned} L_\xi &= 1 + \frac{3B}{4A}\xi_x \Delta t \frac{\partial}{\partial\xi} - \xi_x \frac{\Delta t^2}{2A}\frac{\partial}{\partial\xi} F_1 \frac{\partial}{\partial\xi} \\ L_\eta &= 1 - \xi_x \frac{\Delta t^2}{2A}\frac{\partial}{\partial\eta} F_2 \frac{\partial}{\partial\eta} \\ L_\varsigma &= 1 - \xi_x \frac{\Delta t^2}{2A}\frac{\partial}{\partial\varsigma} F_3 \frac{\partial}{\partial\varsigma} \end{aligned} \tag{34}$$

The equations for the spatial fluxes F_1, F_2, F_3, and the residual R are given in Ref 11. In Eq. (33) σ is a relaxation parameter which is normally set equal to 1.0. To accelerate convergence to steady-state, the residual R may be over-relaxed using $\sigma > 1$. Equation (33) is solved using three sweeps through the grid by sequentially applying the operators L_ξ, L_η, and L_ς as

$$\begin{aligned} \xi - sweep: \; & L_\xi \Delta\phi^* = -\sigma R \\ \eta - sweep: \; & L_\eta \Delta\phi^{**} = \Delta\phi^* \\ \varsigma - sweep: \; & L_\varsigma \Delta\phi = \Delta\phi^{**} \end{aligned} \tag{35}$$

Further details of the algorithm development and solution procedure may be found in Refs. 11 and 12.

The CAP-TSD code can be used for aerodynamic and aeroelastic analysis of complete aircraft configurations with arbitrary combinations of lifting surfaces and bodies including canard, wing, tail, control surfaces, tip launchers, pylons, fuselage, stores, and nacelles. The code has the option of half-span modeling for symmetric cases or full-span modeling to allow the treatment of anti-symmetric mode shapes, fuselage yaw, or unsymmetric configurations such as an oblique wing or unsymmetric wing stores.

TWO-DIMENSIONAL RESULTS

For two-dimensional study, the NACA 0012 airfoil was selected for analysis because of the simplicity of the geometry and the availability of experimental unsteady data.[13] Steady-state calculations were performed for the airfoil at $M_\infty = 0.8$ and $\alpha_0 = 1.25°$. These conditions correspond to an AGARD test case for inviscid flow methods,[14] and have been studied by numerous researchers. Unsteady calculations were performed for the airfoil pitching harmonically about the quarter chord with an amplitude of $\alpha_1 = 2.51°$ and a reduced frequency of k=0.1628 ($k = \frac{\omega c}{u}$) at $M_\infty = 0.755$ and $\alpha_0 = 0.016°$. These calculations are compared with the experimental unsteady data of Ref. 13.

Steady Flow

The effects of grid density were determined first, using the Euler code, by examining the force and moment coefficients as well as the pressure distribution as the grid was systematically refined. For this study, three C-type grids were considered. The finest grid was a 257 × 65 mesh with 257 points along the surface and wake, with 176 points on the airfoil surface and 65 points approximately normal to the surface. The coarsest grid was constructed by deleting every other mesh line from the finest grid resulting in a 129 × 33 mesh with 88 points on the airfoil. An intermediate 193 × 41 mesh was also used which had 112 points on the airfoil. For all of the grids, the outer boundary radius was fixed at approximately 20 chordlengths.

The effects of grid density on the lift, moment, and drag coefficients are shown in Fig. 1. The results are plotted as coefficient versus 1/(total number of grid points) for three values of κ, which controls the spatial accuracy of the upwind FVS scheme. The calculations included a point vortex representation for the airfoil to account for the induced velocities in the far field due to circulation (lift). As the grid density was increased the values of the lift, moment, and drag coefficients extrapolate to 0.3606, -0.0395, and 0.0229, respectively, for all values of κ. With the third-order upwind-biased scheme ($\kappa = 1/3$), the lift and moment coefficients are relatively insensitive to grid density as shown in the upper part of Fig. 1. The solution obtained using Fromm's scheme ($\kappa = 0$) shows slightly more variation in these coefficients as the grid density is decreased. The second-order fully upwind scheme ($\kappa = -1$) exhibits the largest change between the fine and coarse grid solutions. For the drag coefficient, all three schemes yield approximately the same results. With the third-order upwind-biased scheme, the lift and drag coefficients on the 257 × 65 mesh differ from the extrapolated values by 0.04 percent and 1.38 percent, respectively. On the 193 × 41 mesh the values of lift and drag differ by 0.10 percent and 3.9 percent of the extrapolated values. For both the fine and the medium grids, the moment coefficient is within 0.1 percent of the value extrapolated for infinite mesh density. On the 129 × 33 mesh, the lift, moment, and drag coefficients show a 0.175 percent, 0.58 percent, and 6.8 percent difference from the extrapolated values, respectively.

The effects of grid density on the pressure distribution are shown in the top third of Fig. 2. These results were obtained using the third-order scheme for the three grids previously described. The pressure distributions computed using the three grids are almost identical with only slight differences near the upper and lower surface shocks.

The effect of including the point vortex induced velocities in the far field boundary conditions on the solution is shown in the center of Fig. 2. The calculations were performed using the 193 x 41 grid and results were obtained both with and without including the point vortex. The resulting pressure distributions are very similar with small differences occurring only near the shocks. The effect on the force and moment coefficients, however, is more significant. For example, the lift coefficient decreases from the previously reported value of 0.3606, computed with the point vortex, to a value of 0.3428 computed without it. It is noted that in Ref. 15, Euler solutions for airfoils were obtained which were virtually independent of the outer boundary extent when the point vortex velocities were included in the far field boundary condition.

Finally, a comparison between Euler and TSD potential flow pressure distributions for this case is presented in the lower third of Fig. 2. Both sets of results were obtained by neglecting the vortex induced velocities in the far field. The Euler calculation was performed using the 193 x 41 grid. The TSD calculation was performed on a Cartesian grid which was derived from the Euler grid by using the distribution of points along the airfoil projected to the mean plane and using the (approximately) vertical distribution of points at the trailing edge. As shown in Fig. 2, the two solutions are in very good agreement, with the main differences occuring in the regions of the shocks. The shocks are slightly sharper in the Euler solution, which has only one interior point in each of the shocks, in comparison with the TSD solution. Furthermore, this case is a very challenging one for the TSD code since it is normally regarded as being outside the range of applicability of TSD potential theory. The good agreement is attributable to the inclusion of entropy and vorticity effects as demonstrated in Ref. 7.

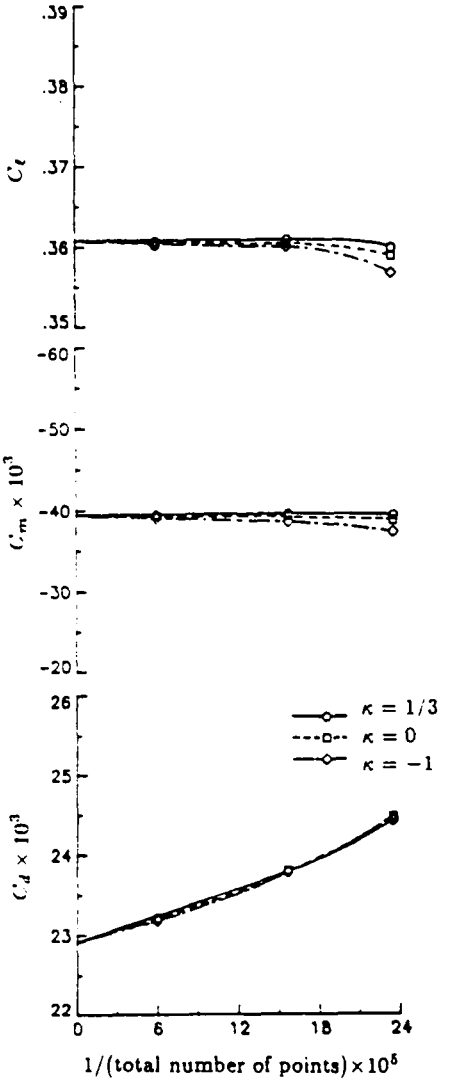

Figure 1. Effects of grid density and spatial accuracy on the force and moment coefficients for the NACA 0012 airfoil at $M_\infty = 0.8$ and $\alpha_0 = 1.25°$ computed using the CFL3D code.

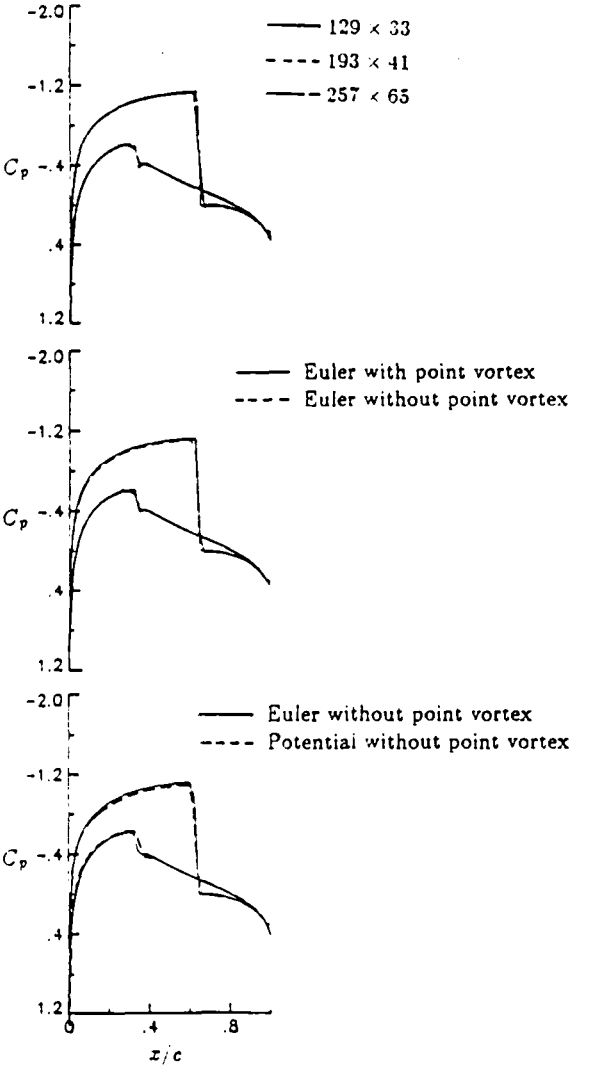

Figure 2. Effects of grid density and far field boundary conditions on the pressure distribution for the NACA 0012 airfoil at $M_\infty = 0.8$ and $\alpha_0 = 1.25°$.

Unsteady Flow

Results were obtained for the pitching NACA 0012 airfoil using both the Euler and potential codes. The Euler results were obtained using the 193 × 41 grid and the third-order upwind-biased scheme ($\kappa = 1/3$). The grid for the potential flow calculations was derived from the Euler grid as described previously. For both Euler and TSD, the results were obtained using second-order time accuracy and two subiterations at each time step, unless otherwise noted. Furthermore, the Euler and TSD solutions did not use the point vortex far field boundary condition since the steady-state lift is nearly zero for this case.

Calculated instantaneous pressure distributions at eight points in time during a cycle of motion are shown in Fig. 3 for comparison with each other as well as with the experimental data. In each pressure plot, the instantaneous angle of attack is noted. Both sets of calculations were performed using 1000 steps per cycle of motion to ensure temporal convergence. During the first part of the cycle, there is a shock wave on the upper surface of the airfoil and the flow over the lower surface is predominately subcritical. During the latter part of the cycle, the flow about the upper surface is subcritical and a shock forms along the lower surface. The pressure distributions indicate that the shock position oscillates over approximately 25 percent of the chord, and in general, that the two sets of calculated results compare well with the data with notable exceptions near the shocks. Furthermore, the shock from the potential solutions is generally located slightly downstream of the Euler shock. This result is somewhat surprising given the near perfect agreement in shock location for the steady case shown in Fig. 2.

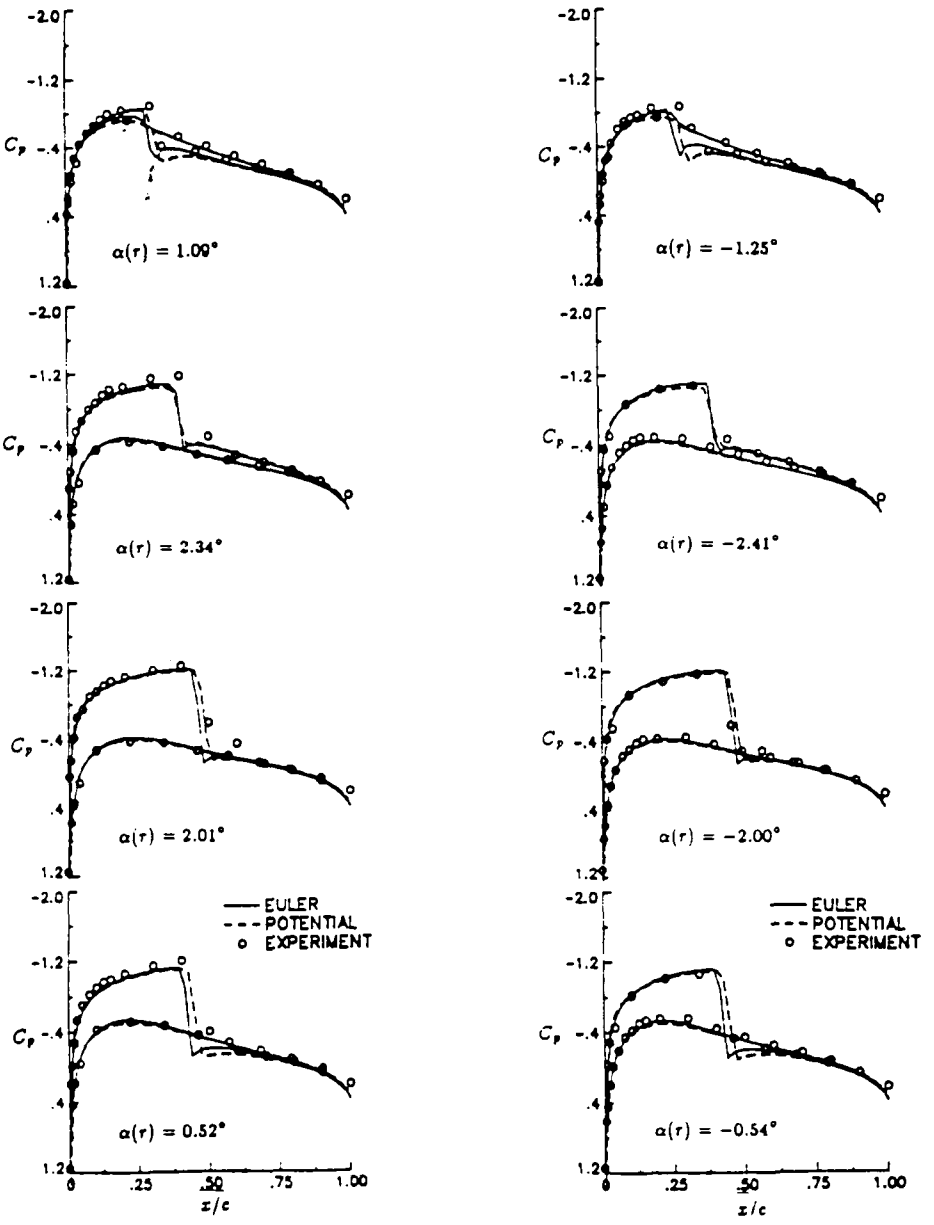

Figure 3. Comparison of instantaneous pressure distributions for the NACA 0012 airfoil at $M_\infty = 0.755, \alpha_0 = 0.016°, \alpha_1 = 2.51°$, and k = 0.1628.

Effects of reduced frequency on the first harmonic components of the upper surface pressure distributions are shown in Fig. 4. The results are presented as real and imaginary parts of the first harmonic of the pressure coefficient, normalized by the amplitude of motion. Potential flow results were obtained using 1000 steps per cycle of motion for k=0.1628, 0.3256, 0.6512, and 1.3024. Euler results for k=0.1628 were also obtained using 1000 steps per cycle while 500 steps per cycle were used for the other three frequencies. Comparisons between Euler and potential solutions are presented for all four values of k. Experimental data is available at k=0.1628 to assess the accuracy of the calculations. As shown in Fig. 4, the two sets of calculations agree equally well across the frequency range considered and are also in good agreement at k=0.1628 with the experimental unsteady pressure data.

Effects of time-step size were also investigated by obtaining results for a wide range of Δt using both the Euler and potential codes. These results are partly summarized in Fig. 5 in the form of lift and moment coefficients versus the instantaneous angle of attack during a cycle of motion, for the four values of k that were considered previously. Euler results are shown in Fig. 5(a); TSD potential results are shown in Fig. 5(b). The calculations were performed with as many as 1000 steps per cycle and with as few as 25. In each case, two subiterations were used at each time step. The Euler and TSD coefficients are generally very similar due to the similarity in the pressure distributions already shown. At k=0.1628, the Euler and TSD coefficients compare reasonably well with each other and with the experimental data. At the higher reduced frequencies, however, small differences between the two sets of results are apparennt. For example, at k=1.3024 the phase lag in the Euler lift coefficient is less than that in the TSD lift coefficient. Also at k=0.6512 and 1.3024, the TSD moment coefficients have a slightly greater magnitude in comparison with the Euler moment coefficients. Furthermore, the results indicate that generally much less than 1000 steps per cycle of motion were required to obtain temporally converged solutions depending on the reduced frequency. At the higher k-values, fewer steps per cycle of motion were required. At the lower frequencies, a larger number of steps were required to accurately resolve the unsteadiness of the flow. When too few steps per cycle were used, small differences appear in the lift and moment coefficients. The differences in the moment coefficients are slightly larger than the differences in the lift coefficients. These differences occur because of numerical oscillations which form near shock waves as shown in Fig. 6, computed using the Euler code. These oscillations are a further indication of an insufficient resolution of the solution in time.

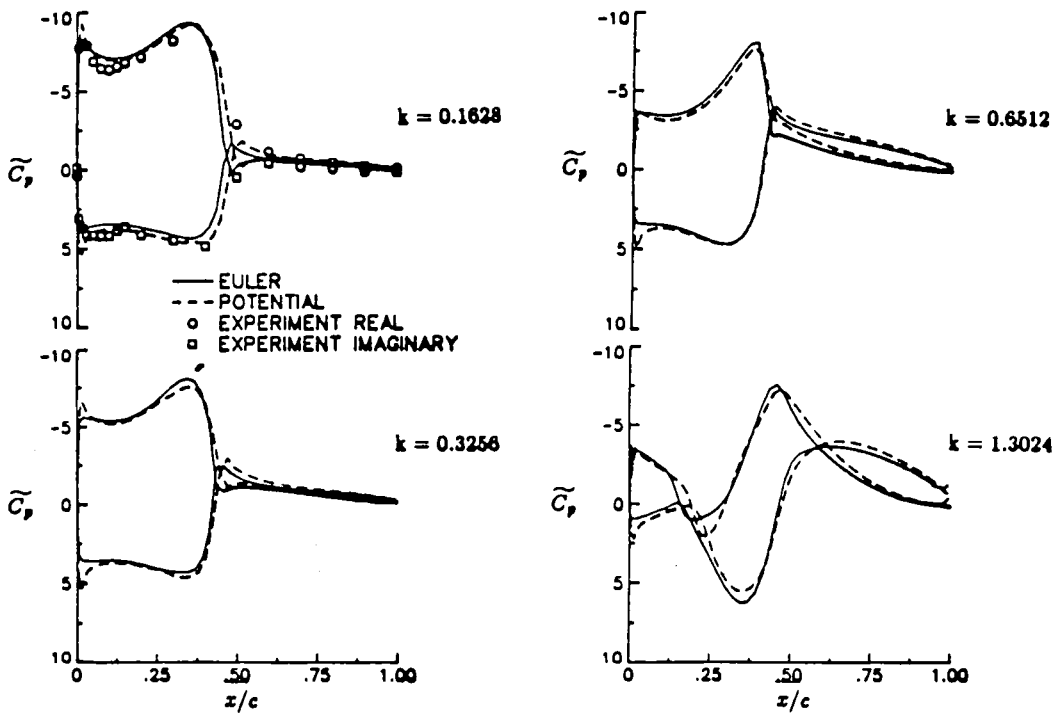

Figure 4. Effects of reduced frequency on first harmonic components of the upper surface pressure distributions for the NACA 0012 airfoil at $M_\infty = 0.755$, $\alpha_0 = 0.016°$, and $\alpha_1 = 2.51°$.

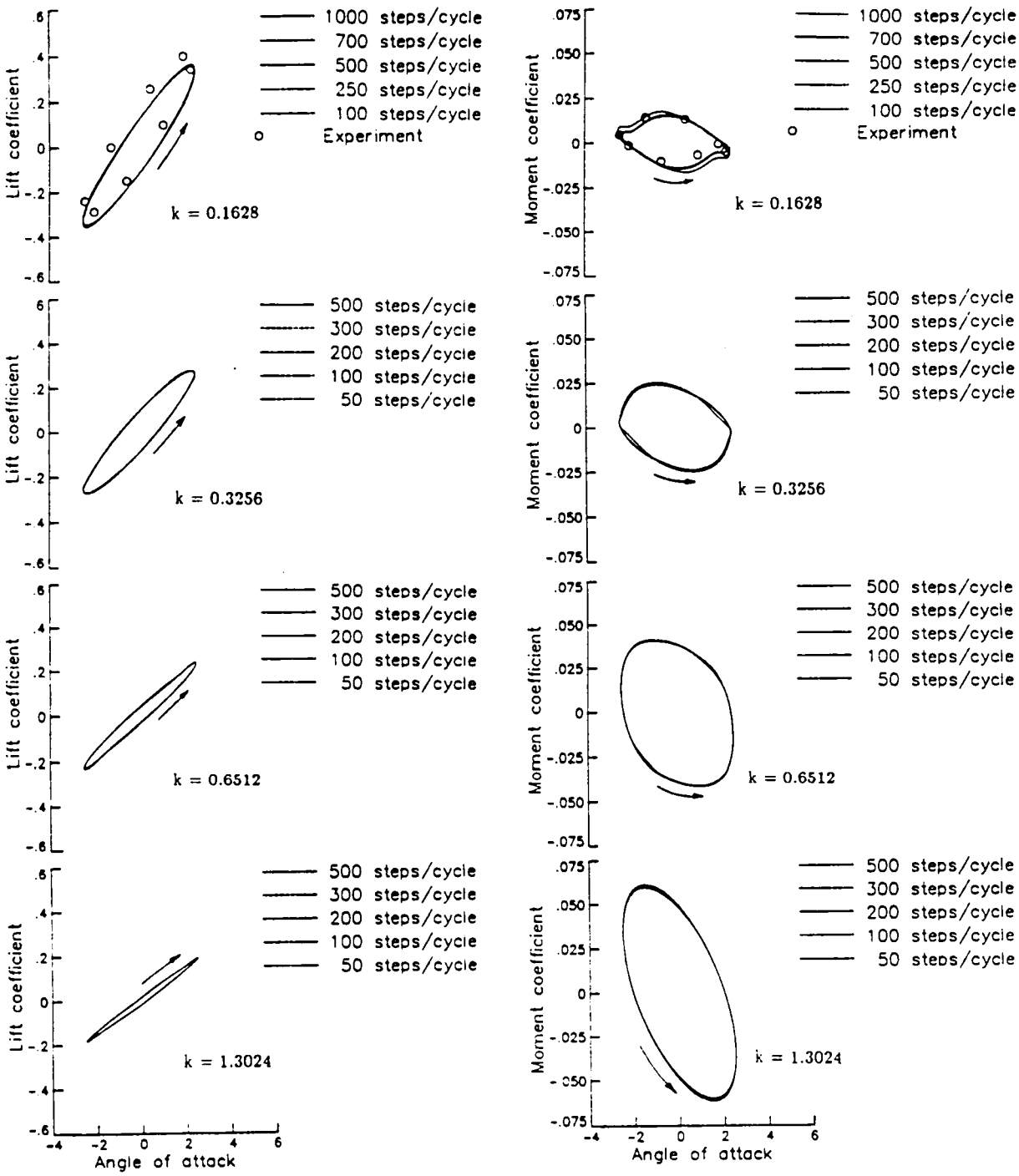

(a) Euler.

Figure 5. Effects of time-step size and reduced frequency on the lift and moment coefficients versus instantaneous angle of attack for the NACA 0012 airfoil at $M_\infty = 0.755$, $\alpha_0 = 0.016°$, and $\alpha_1 = 2.51°$.

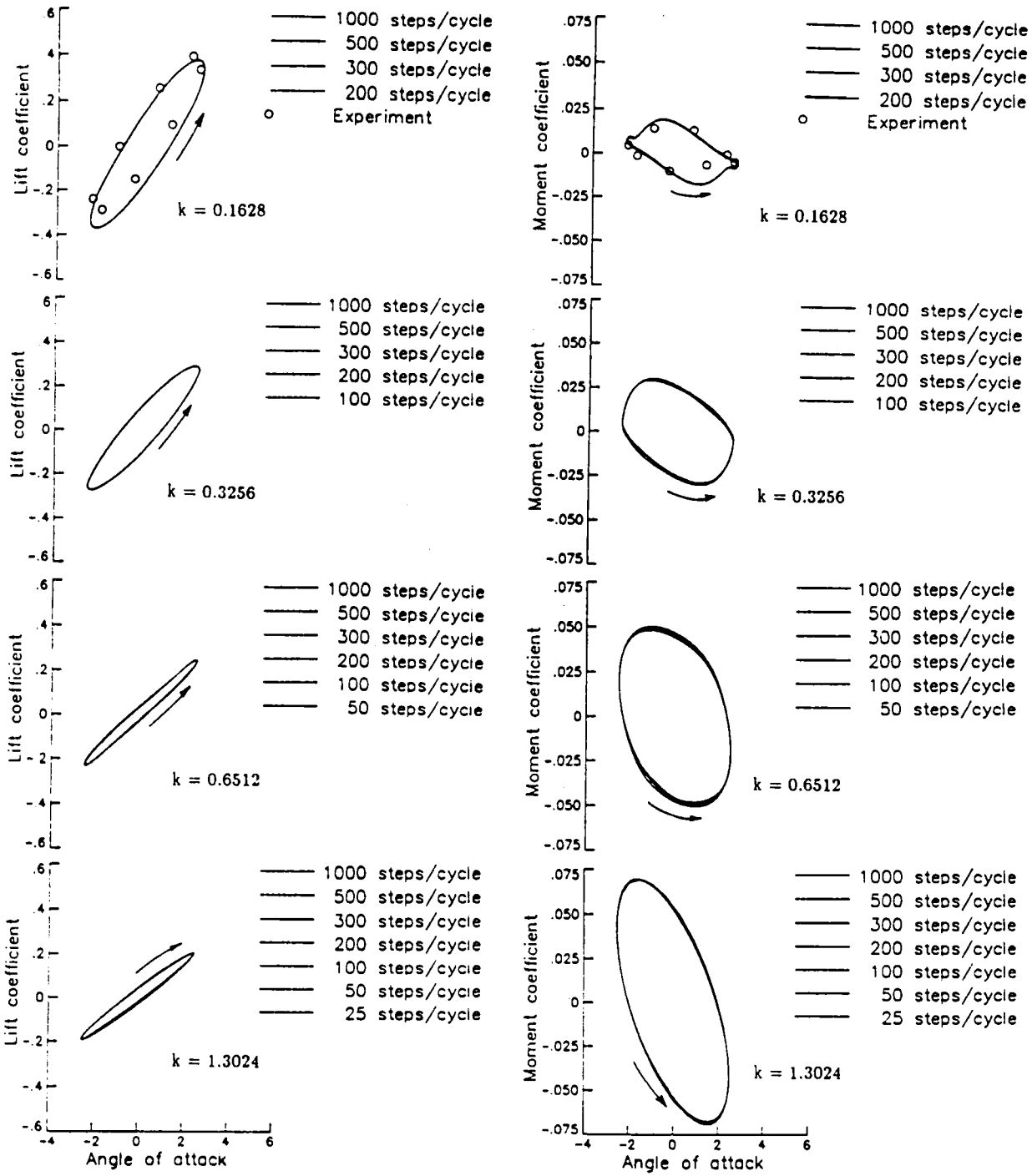

(b) Potential.

Figure 5. Concluded.

To examine this effect more closely, the average total variation of the pressure coefficients over a cycle of motion was computed using the Euler code for various numbers of steps per cycle of motion. The average total variation (TV_a) over a cycle was defined by

$$TV_a = \frac{1}{N}\Sigma_n\Sigma_i(|\, c_p(i+1) - c_p(i)\,|) \tag{36}$$

where N is the total number of steps per cycle and the summations Σ_i and Σ_n are over the number of grid points on the surface of the airfoil and over the number of time steps in the cycle, respectively. Since the total variation gives an indication of how much the pressure increases and decreases over the airfoil, numerical oscillations in the solution can be detected by a higher average total variation over a cycle of motion. Figure 7 shows the average total variation versus the number of steps per cycle for three values of reduced frequency. As the number of points per cycle is increased, the average total variation asymptotes to a particular value indicating that sufficient temporal convergence has been achieved. The number of steps per cycle required to adequately resolve the flow unsteadiness increases as the reduced frequency decreases. It is important to note however that although fewer time steps per cycle are required as the reduced frequency is increased, the actual time step required decreases. For example, from Fig. 7 it is seen that for a reduced frequency of 0.1628, good results can be expected with 300 steps per cycle corresponding to a time step of approximately 0.17. For a reduced frequency of 1.3024, a time step of this size yields less than 50 points in the cycle which is clearly seen in Fig. 7 to be insufficient. This result is not surprising since the higher frequency case should require smaller time steps to resolve the physics of the flow.

Finally, the effects of performing subiterations at each time step on the Euler solutions were investigated as shown in Fig. 8. The pressure distributions were obtained with and without subiterations using 1000 steps per cycle of motion. As shown in the figure, the results obtained without using subiterations are slightly different in the shock region from those obtained with two subiterations at each time step. If the number of steps per cycle is increased to 1700, then Fig. 9 shows that the pressure distribution obtained without subiterations agrees closely to the previous results obtained using two subiterations. The influence of the subiterations is therefore to decrease the number of steps required to sufficiently resolve a cycle of motion. This gain, however, may be offset by the additional work required at each step.

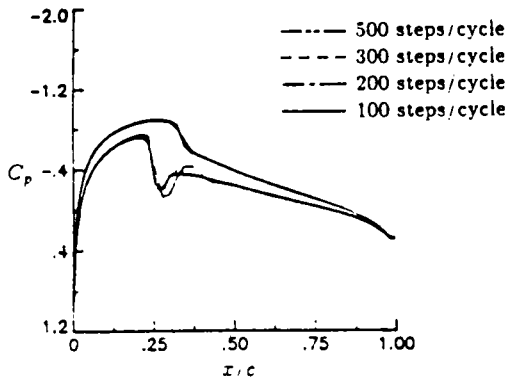

Figure 6. Effect of step size on the instantaneous pressure distribution for the NACA 0012 airfoil at $M_\infty = 0.755$, $\alpha_0 = 0.016°$, $\alpha_1 = 2.51°$, and k = 0.3256.

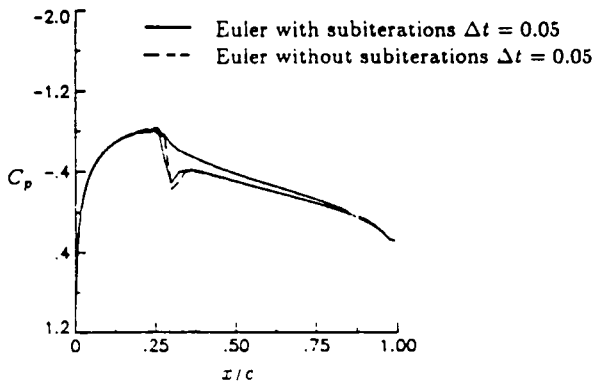

Figure 8. Effect of performing subiterations on the instantaneous pressure distribution at $\alpha(r) = -1.25°$.

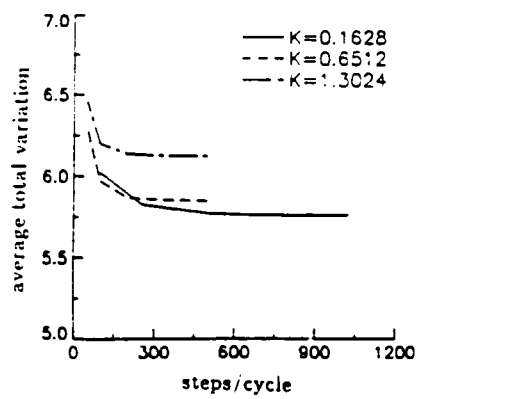

Figure 7. Average total variation versus the number of steps per cycle for three values of reduced frequency for the NACA 0012 airfoil.

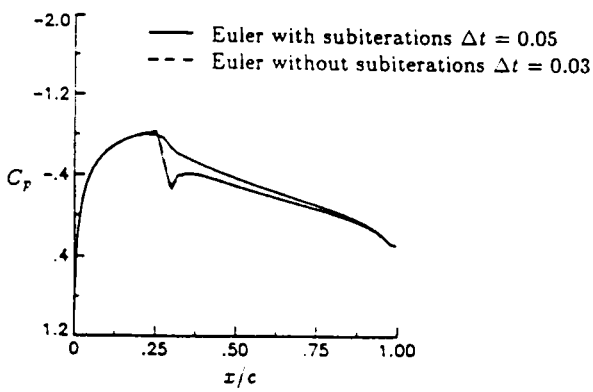

Figure 9. Instantaneous pressure distributions which illustrate the comparison between using a small step size with no subiterations and using a larger step size with subiterations.

THREE-DIMENSIONAL RESULTS

For three-dimensional study, the F-5 fighter wing was selected for analysis because of the availability of both steady and unsteady data to assess the accuracy of the calculations. The F-5 wing has a panel aspect ratio of 1.58, a leading edge sweep angle of 31.9°, and a taper ratio of 0.28. The airfoil section is a modified NACA 65A004.8 airfoil which has a drooped nose and is symmetric aft of 40 percent chord. The calculations are compared with the experimental pressure data from an F-5 wing model tested by Tijdeman, et al.[16] Steady calculations were performed at $M_\infty = 0.95$ and 0.90, for the wing at zero degrees angle of attack; conditions which have also been studied by other researchers. Unsteady calculations were performed at $M_\infty = 0.9$ for the wing pitching harmonically about a line perpendicular to the root midchord. The amplitude of motion was selected as $\alpha_1 = 0.109°$ and the reduced frequency (based on root chord) was k=0.274 for comparison with the experimental pressure data of Ref. 16. It is noted that the amplitude is very small which may influence the accuracy of the experimental data and that the wing model had some small aeroelastic deformation which was not accounted for in the calculations.

Steady Flow

Similar to the NACA 0012 airfoil study, the effects of grid density on the steady pressure distributions of the F-5 wing at $M_\infty = 0.95$ were determined using the Euler code. Three successively finer grids were used and the pressure distributions are compared with each other as well as with the experimental data. The finest grid is a 257 × 65 × 65 mesh which has 176 points on the wing surface in the streamwise direction, 65 points normal to the surface, and 65 points in the spanwise direction with 33 spanwise points on the wing. A medium grid consisted of a 193 × 33 × 41 mesh with 112 points on the wing surface in the streamwise direction, 33 points normal to the surface, and 20 points on the wing in the spanwise direction. The coarsest grid, which was a 129 × 33 × 33 mesh, was constructed by deleting every other mesh line from the finest grid.

Figure 10(a) shows steady pressure distributions obtained using the 129 × 33 × 33 (coarse) and 257 × 65 × 65 (fine) grids at three span stations of y/s=0.18, 0.51, and 0.88, where y is the direction along the span and s is the span of the wing. The two sets of calculated results agree fairly well with each other except along the upper surface near the leading edge which indicates that the 129 × 33 × 33 grid is too coarse and that grid refinement is necessary. Solutions obtained using the 193 × 33 × 41 (medium) and 257 × 65 × 65 (fine) grids are compared in Fig. 10(b). At each of the three span stations, the calculated pressure distributions agree closely with one another at all points on the wing surface including the leading edge region. This indicates that both grids provide adequate grid resolution and that the results would not change appreciably by the addition of more grid points. Therefore, the 193 × 33 × 41 grid is adequate for obtaining spatially converged solutions for the F-5 wing at these conditions. Furthermore, the calculated pressures agree with the experimental data in regions away from the shocks. The computed shocks, however, lie aft of the experimental shock locations indicating that viscous effects may be important for this case.

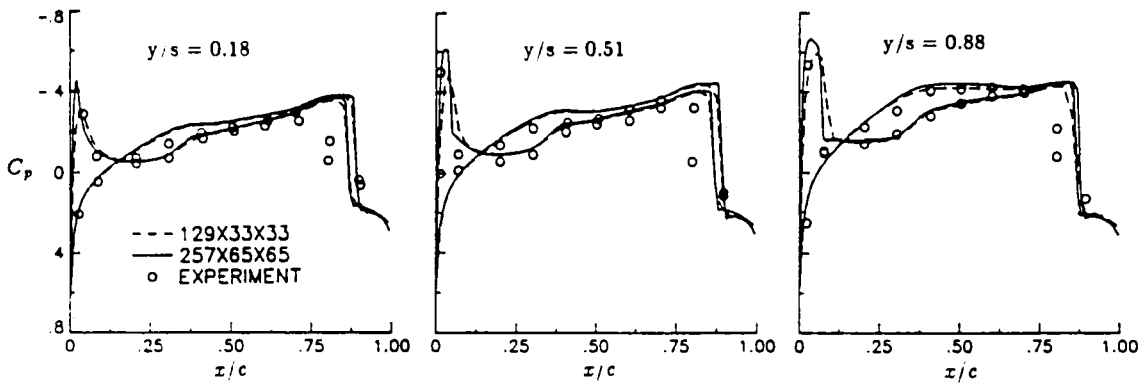

(a) coarse and fine mesh solutions.

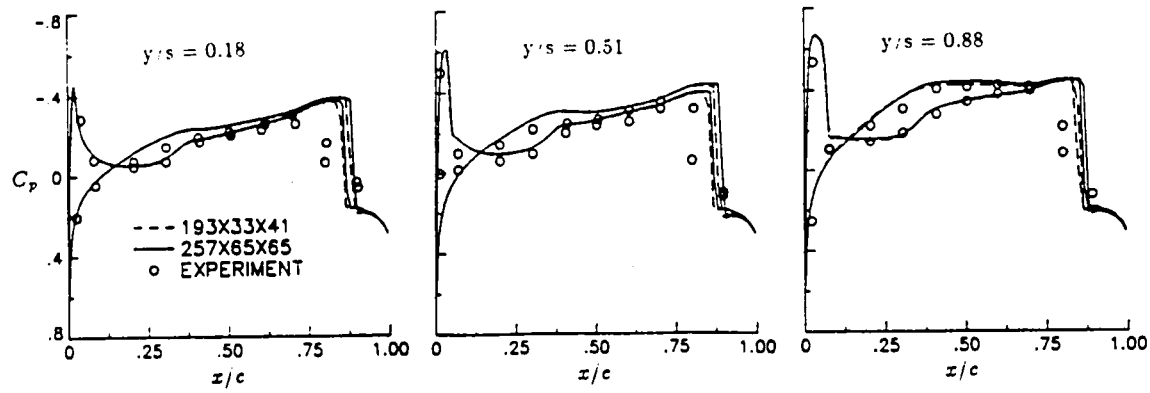

(b) medium and fine mesh solutions.

Figure 10. Effect of grid density on the steady pressure distributions for the F-5 wing at $M_\infty = 0.95$ and $\alpha_0 = 0.0°$ computed using the CFL3D code.

Steady pressure distributions obtained using both Euler and TSD are compared with the experimental data in Fig. 11 for the F-5 wing at $M_\infty = 0.90$. The grid used for the Euler calculation was the 193 × 33 × 41 mesh. For the potential flow calculations, the grid was constructed in a similar manner as was done for the NACA 0012 airfoil. For all three span stations along the wing, the agreement between the Euler and potential flow results is excellent on the lower surface of the wing including the leading edge suction peak. Along the upper surface of the wing, there is a mild shock wave that is similarly predicted by the Euler and potential codes, although the potential flow results show slightly more negative pressures upstream of the shock than the Euler results. The two sets of calculated results generally compare well with the experimental data especially along the lower surface of the wing. The data, however, does not indicate the presence of the mild shock wave on the upper surface at y/s=0.18 and 0.51 which is predicted by the calculations.

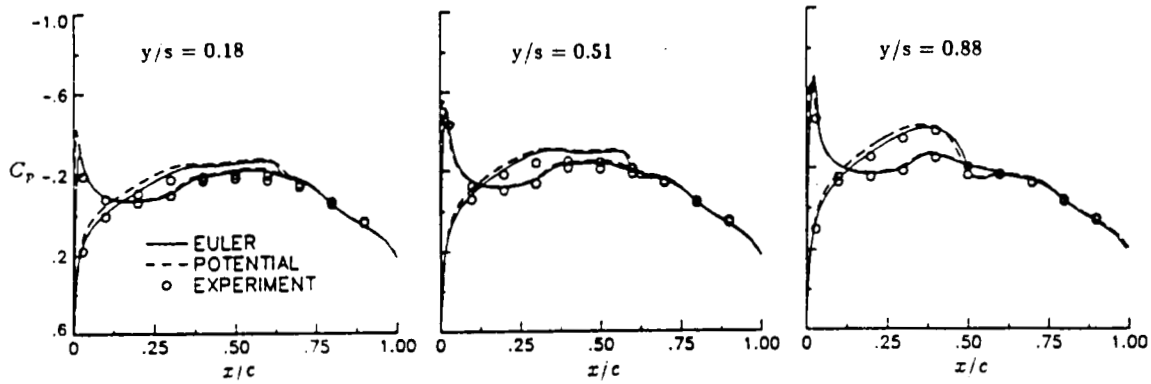

Figure 11. Comparison of steady pressure distributions for the F-5 wing at $M_\infty = 0.9$ and $\alpha_0 = 0.0°$.

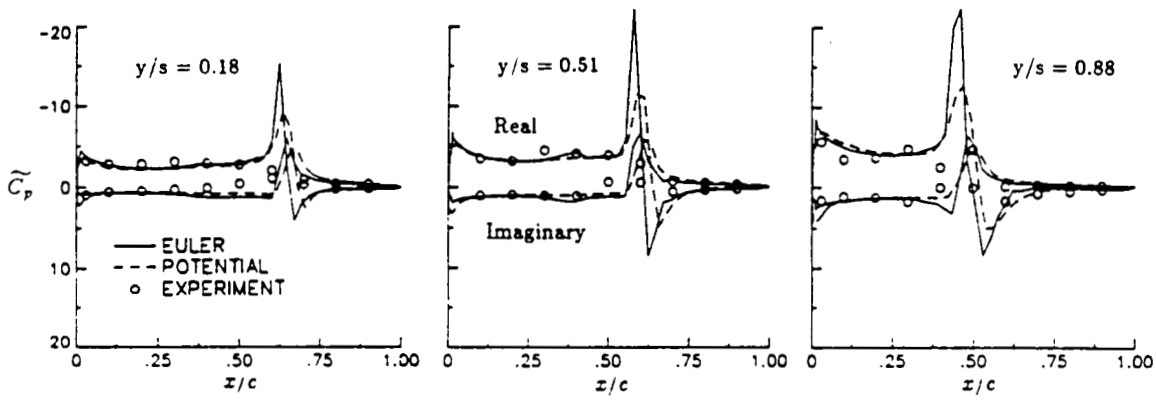

(a) upper surface.

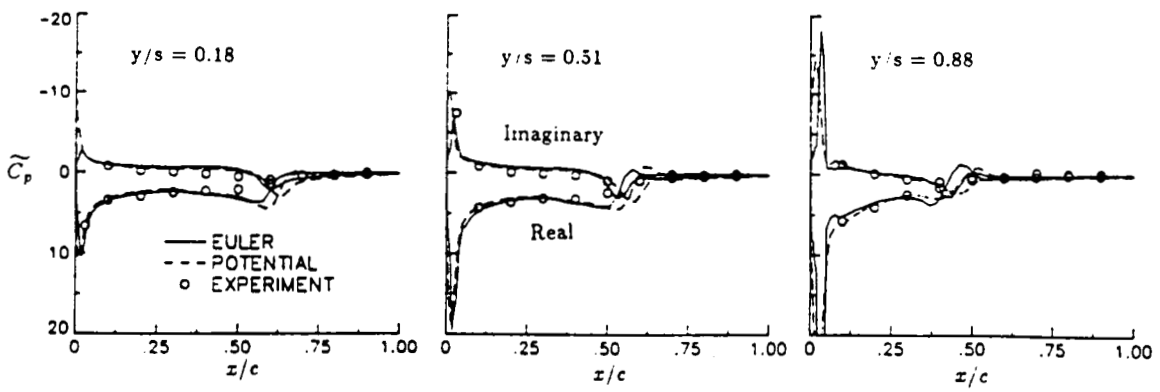

(b) lower surface.

Figure 12. Comparison of first harmonic components of the pressure distribution for the F-5 wing at $M_\infty = 0.9, \alpha_0 = 0.0°, \alpha_1 = 0.109°$, and k = 0.274.

Unsteady Flow

Results were obtained for the pitching F-5 wing using both the Euler and potential codes. The Euler calculations were performed using first order time accuracy, no subiterations, and slightly more than 1000 steps per cycle of motion. The potential flow calculations were performed using second-order time accuracy, two subiterations at each time step, and 300 steps per cycle of motion. Figure 12 shows the real and imaginary components of the unsteady pressure distributions at the same three span stations as the steady results of Fig. 11. Unsteady pressures along the upper surface are shown in Fig. 12(a); unsteady pressures along the lower surface are shown in Fig. 12(b). On the upper surface there is a shock pulse in the calculated pressure distributions near 50-60 percent chord which is produced by the motion of the shock wave. The experimental data does not show a shock pulse in the pressures at the two inboard stations because of the absence of the steady shock as discussed above. On the lower surface there are positive and negative spikes in the real and imaginary pressure distributions, respectively, which are much more pronounced in the outboard region of the wing. These spikes are produced by an embedded region of supersonic flow, as indicated by the lower surface leading edge suction peaks shown previously in Fig. 11. In general, the two sets of calculated pressures agree well except near the upper surface shock pulse and in the midchord region along the lower surface. These differences may be attributed to the sharper shock capturing ability of the Euler code in comparison with that from the TSD code. Also, comparisons with the experimental data are qualitatively good for both the Euler and potential results. Further work is required to sort out the differences between the two sets of calculations, however, and additional correlations with experimental data are necessary to validate both codes.

CONCLUDING REMARKS

A code validation study has been presented involving the CFL3D Euler code and the CAP-TSD transonic small-disturbance code for both steady and unsteady applications. The purpose of the evaluation was to determine the accuracy and applicability of the methods by performing detailed studies to assess the influence of several parameters in the numerical modeling of the solution. Two-dimensional parameter studies for steady flow applications were conducted to determine the effects of grid density, spatial accuracy, and far field boundary conditions. The case considered was a NACA 0012 airfoil at a freestream Mach number of 0.8 and an angle of attack of 1.25 degrees. It was found that as the grid was refined, the third-order upwind biased calculation showed less sensitivity than either of the two second-order methods as expected. The values of the lift and drag coefficients on the finest grid (257×65) differ from the values obtained by extrapolation to infinite mesh size by 0.04 percent and 1.38 percent, respectively. The lift and drag on the medium mesh (193×41) differ by 0.10 and 3.9 percent, respectively. For both the fine and medium meshes, the moment coefficient is within 0.1 percent of the extrapolated value. The effect of including a point vortex representation for the airfoil to account for the induced velocities in the far field boundary conditions exhibited only small changes in the pressure distribution which when integrated over the chord, results in approximately a five percent change in the lift coefficient. For three-dimensional steady flow, a grid refinement study using the Euler equations was conducted on the F-5 fighter wing at $M_\infty = 0.95$ and $\alpha_0 = 0.0°$ using three grids with approximately one million, two-hundred fifty-thousand, and one-hundred forty-thousand mesh points, respectively. It was found that the finest grid and the medium grid resulted in essentially identical results. Comparisons between the Euler and potential flow calculations were made for both two-and three-dimensional cases. For the cases considered, the comparisons were very good.

Unsteady calculations were also performed for forced sinusoidal pitching motion to determine the effects of reduced frequency, time step size, and subiterations performed to minimize linearization and factorization errors. It was determined that fewer time steps per cycle were required to resolve the flow field as the frequency of oscillation was increased. In addition, the influence of using subiterations at each time step is to decrease the number of steps required to sufficiently resolve a cycle of motion. Comparisons for two-and three-dimensional cases between Euler and potential flow calculations were generally good except in the immediate vicinity of the shocks where the potential flow shocks were often located slightly aft of the Euler shocks. This result was somewhat surprising given the excellent agreement between the Euler and TSD calculations for steady flow where the shocks were much stonger.

To asses the applicability of the TSD code, comparisons with Euler calculations for both steady and unsteady flows have been made. The generally favorable agreement between the Euler and TSD calculations indicates that TSD calculations incorporating both entropy and vorticity corrections can be expected to yield results comparable to Euler calculations for problems similar to those considered in the current study. In addition, for TSD calculations, the grid remains fixed for calculating both steady and unsteady flows so that computations over complex configurations are relatively straightforward. Similar calculations with the Euler equations are often complicated by difficult grid generation and by the fact that for unsteady calculations on moving meshes, new grids must be computed at each time step. Also, since the solution of the three dimensional Euler equations involves five unknowns at each grid point, the computer time required for the Euler calculations is much higher than that required by the solution of the TSD equation. For the Euler code used in the present study, the computational rate for three-dimensional calculations was approximately 60×10^{-6} seconds/grid point/iteration while the TSD code required only 5×10^{-6} seconds/grid point/iteration. Both the Euler and TSD calculations were done on a CRAY-2 supercomputer at the National Aerodynamic Simulator facility located at NASA Ames Research Center.

REFERENCES

1. Jameson, A., "Successes and Challenges in Computational Aerodynamics," AIAA 87-1184, January 1987.
2. Edwards, J. W., and Thomas, J. L., "Computational Methods for Unsteady Transonic Flows," AIAA 87-0107, January 1987.
3. Anderson, W. K., Implicit Multigrid Algorithms for the Three-Dimensional Flux Split Euler Equations. PhD. Dissertation, Mississippi State University, August 1986.
4. Anderson, W. K., Thomas, J. L., and Rumsey, C. L., "Extension and Applications of Flux-Vector Splitting to Unsteady Calculations on Dynamic Meshes," AIAA 87-1152-CP, 1987.
5. Anderson, W. K., Thomas, J. L., and Van Leer, B.,"A Comparison of Finite Volume Flux Vector Splittings for the Euler Equations," AIAA Journal, Vol. 24, No. 9, September 1986, pp. 1453-1460.
6. Van Leer, B., Thomas, J. L., Roe, P., and Newsome, R., "A Comparison of Numerical Flux Formulas for the Euler and Navier-Stokes Equations," AIAA 87-1104-CP, 1987.
7. Batina, J.T., "Unsteady Transonic Small-Disturbance Theory Including Entropy and Vorticity Effects," AIAA 88-2278, April 1988.
8. Dang, T.Q., and Chen, L. T., "An Euler Correction Method for Two- and Three-Dimensional Transonic Flows," AIAA 87-0522, January 1987.
9. Batina, J. T., Seidel, D. A., Bland, S. R., and Bennett, R. M., "Unsteady Transonic Flow Calculations for Realistic Aircraft Configurations," AIAA 87-0850, April 1987.
10. Batina, J. T., Seidel, D. A., Bennett, R. M., Cunningham, H. J., and Bland, S. R., "Steady and Unsteady Transonic Small Disturbance Analysis of Realistic Aircraft Configurations," Transonic Symposium, NASA Langley Research Center, Hampton, Virginia, April 1988.
11. Batina, J. T., "An Efficient Algorithm for Solution of the Unsteady Transonic Small Disturbance Equation," AIAA 87-0109, January 1987.
12. Batina, J. T., "Unsteady Transonic Algorithm Improvements for Realistic Aircraft Applications," AIAA 88-0105, January 1988.
13. Landon, R. H., "NACA 0012 Oscillatory and Transient Pitching," Data Set 3 in AGARD-R-702, Compendium of Unsteady Aerodynamic Measurements, August 1982.
14. Yoshihara, H., "Test Cases for Inviscid Flow Field Methods," AGARD-AR-211, May 1985.
15. Thomas, J. L., and Salas, M. D., "Far-Field Boundary Conditions for Transonic Lifting Solutions to the Euler Equations," AIAA Journal, Vol. 24, No. 7, July 1986, pp 1074-1080.
16. Tijdeman, H., Van Nunen, J. W. G., Kraan, A. N., Persoon, A. S., Poestkoke, R., Roos, R., Schippers, P., and Siebert, C. M.,: "Transonic Wind Tunnel Tests on an Oscillating Wing with External Stores," AFFDL-TR-78-194, December 1978.

NASA

Report Documentation Page

1. Report No.	2. Government Accession No.	3. Recipient's Catalog No.
NASA TM-100664		

4. Title and Subtitle
Accurate Solutions, Parameter Studies, and Comparisons for the Euler and Potential Flow Equations

5. Report Date
September 1988

6. Performing Organization Code

7. Author(s)
W. Kyle Anderson
John T. Batina

8. Performing Organization Report No.

10. Work Unit No.
505-63-21-01

9. Performing Organization Name and Address
Langley Research Center
Hampton, Virginia 23665-5225

11. Contract or Grant No.

13. Type of Report and Period Covered
Technical Memorandum

12. Sponsoring Agency Name and Address
National Aeronautics and Space Administration
Washington, DC 20546

14. Sponsoring Agency Code

15. Supplementary Notes
The paper was presented at the AGARD 62nd Meeting of the Fluid Dynamics Panel Symposium on Validation of Computational Fluid Dynamics, Lisbon, Portugal, May 2-5, 1988.

16. Abstract
Parameter studies are conducted using the Euler and potential flow equation models for steady and unsteady flows in both two and three dimensions. The Euler code is an implicit, upwind, finite volume code which uses the Van Leer method of flux-vector-splitting which has been recently extended for use on dynamic meshes and maintains all the properties of the original splitting. The potential flow code is an implicit, finite difference method for solving the transonic small-disturbance (TSD) equations and incorporates both entropy and vorticity corrections into the solution procedure thereby extending its applicability into regimes where shock strength normally precludes its use. Parameter studies resulting in benchmark type calculations include the effects of spatial and temporal refinement, spatial order of accuracy, far field boundary conditions for steady flow, frequency of oscillation, and the use of subiterations at each time step to reduce linearization and factorization errors. Comparisons between Euler and potential flow results are made as well as with experimental data where available.

17. Key Words (Suggested by Author(s))
Computational Fluid Dynamics
Euler Equations
Potential Flow Equations
Unsteady Aerodynamics

18. Distribution Statement
Unclassified - Unlimited
Subject Category - 02

19. Security Classif. (of this report)	20. Security Classif. (of this page)	21. No. of pages	22. Price
Unclassified	Unclassified	17	A02